J. Fluid Mech. (1982), *vol.* 116, *pp.* 343–362
Printed in Great Britain

Turbulence in two-phase dispersed flows

By T. G. THEOFANOUS AND J. SULLIVAN
Purdue University, W. Lafayette, Indiana 47906

(Received 19 December 1980 and in revised form 14 July 1981)

Turbulence measurements in dispersed-bubble two-phase pipe flow, using laser velocimetry techniques, are presented. The turbulence-intensity measurements show a strong dependence on the quality of the flow. A theoretical basis for the prediction of turbulence levels in two-phase flows is proposed. The approach is applied to dispersed-gas/liquid (bubbly) and solid/gas (particulate) two-phase flows, for which experimental data are available, with excellent results.

1. Introduction

Sufficiently general and rigorous formulations for the calculation of transient two-phase flows are presently available. The numerics of such calculations for large systems also appear to be well at hand. The results of these calculations depend on the phase-interaction models utilized, or the so-called 'constitutive laws'. In fact, it would not be an oversimplification to say that any gains in predictive capability attained by these advanced tools will depend on the generality of the available phase-interaction models. There is significant incentive, therefore, for such generality, which can only be achieved by means of physically realistic, fundamentally oriented, models.

Most two-phase flows of interest are highly turbulent. Physically realistic phase-interaction models, therefore, must account explicitly for the role of turbulence. Turbulence directly affects heat- and mass-transfer rates at solid/fluid and fluid/fluid interfaces (Theofanous, Houze & Brumfield 1976*a*; Theofanous 1980), but it also controls dispersion within the flow field and it may be responsible for flow-regime development. For example, the mechanisms for turbulence-induced phase break-up are well known (Hinze 1955), and recently (Drew & Lahey 1978) turbulence has been related analytically to radial phase separation in vertical pipe flows. On the other hand, the presence and configuration of the gaseous (or solid particulate) phase could significantly affect the turbulence structure of the liquid (or gas). This was demonstrated experimentally, for slurry flows, by Kada & Hanratty (1960). The increase in turbulent dispersion in the continuous phase was used as a measure of the increase in the turbulence level due to the presence of the solid particulate, and such increases were related qualitatively to the increase in the rate of energy dissipation.

Nevertheless, very little is known experimentally about the turbulence aspects of two-phase flows. Limited experimental data have been presented by Jeffries, Scott & Rhodes (1969*a*, *b*), by Theofanous (1975), Theofanous *et al.* (1976*b*) and Akai, Inoue & Aoki (1975) on stratified, horizontal, gas/liquid channel flows, and by Serizawa, Katuoka & Michiyoshi (1975*a*, *b*, *c*) and Lee & Durst (1980) for dispersed-gas/liquid (bubbly) and solid/gas (particle) flows respectively.

The state of the art is such that certain peculiarities and inconsistencies among the data of different investigators are still in the process of resolution. For example, the early data in stratified flows exhibited a peculiar augmentation of the solid/gas interface friction factor (Theofanous 1975; Akai *et al.* 1975; Akai *et al.* 1980). However, based on subsequent, more-detailed experimental information, including direct measurement of the shear-stress distribution in the gas phase, we have demonstrated (Houze & Theofanous 1980) that the reported peculiarity was an artifice due to the non-coincidence of the zero-shear plane and the maximum point in the mean-velocity profiles in such asymmetric flows. Hence, contrary to the well-accepted procedure (i.e. Cohen & Hanratty 1968) it is incorrect to utilize the maximum point in reducing data for interfacial shear and friction factors; rather, the zero-shear plane must be located directly. The dispersed-flow turbulence data also reveal a rather substantial controversy. Namely, the data of Serizawa *et al.* indicate that the turbulence intensity is not strongly affected by the presence and amount of gas flow while the data of Lee & Durst and our own data reveal a major effect. The purpose of this paper is to provide some additional insight to help in putting this controversy into perspective.

2. Experimental facilities

The two-phase flow system consists of a vertical glass pipe, of 57 mm inside diameter, with an inlet plenum and outlet reservoir as shown in figure 1. Nitrogen is introduced into the plenum through ten 0·33 mm diameter holes. Tap water is used as the source, since the single-pass arrangement avoids vibration and gas-separation problems. The measuring station is 24 diameters downstream of the entrance to assure fully developed flow.

The laser–Doppler velocimeter (LDV) employed is a conventional dual scatter-or-fringe type of system (Durst, Melling & Whitelaw 1976). An Argon ion laser (Coherent Radiation Inc.) and home-made LDV arrangement (zoom lens set at 17·78 cm focal length and TSI photomultiplier) were utilized. In the present set up, the velocimeter measures a single component of the velocity vector by measuring the frequency of the scattered light as a particle moves through the fringe pattern. Rotation of a beam splitter in the system rotates the fringe pattern, making the system sensitive to the axial component of velocity or that at $\pm 45°$ to the axial component. The angle between the two transmitted beams is 15·9°, which, along with beam-expansion techniques, gives a probe volume size of approximately 0·05 mm in diameter and 0·25 mm long. The scattering particles are naturally occurring contaminants of the tap water.

A TSI counter processor (model 1990) is used to convert the LDV signal from the photomultiplier tube to an analog signal proportional to velocity. The analog signal is displayed on an oscilloscope and is input to a minicomputer for digital processing. The computer is a DECLAB 11/03 Model with 20K of memory, 16-channel analog-to-digital converter, and dual floppy discs for program and data storage.

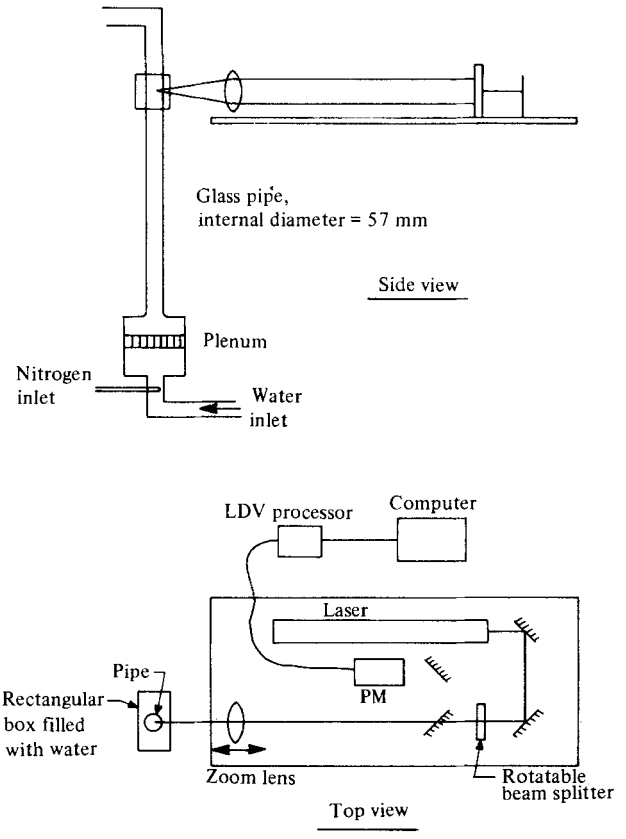

FIGURE 1. The experimental layout.

3. Experimental procedures and data-analysis techniques

Once the data from the LDV processor are in the memory of the computer, standard FORTRAN programming is used to calculate the mean liquid velocity and turbulence intensities. The mean axial velocity and turbulence intensity are calculated using

$$U = \frac{\sum_{i=1}^{N} u_i}{N}, \tag{1}$$

$$u' = \left[\frac{\sum_{i=1}^{N} (u_i - U)^2}{N-1}\right]^{\frac{1}{2}}, \tag{2}$$

respectively, where u_i is the instantaneous axial velocity for the ith data point and N is the number of data points in the digital sample ($N > 4000$). It is well known that the above formulae give rise to a bias in both the mean velocity and turbulence intensity. McLaughlin & Tiederman (1973) provide estimates for the errors; for the present experiments, errors less than 10% are expected. The tangential intensity v' was found using the method established by Yanta & Smith (1973) for turbulent flow.

The turbulence intensity in the axial direction and in directions $\pm 45°$ to the mean are measured. The tangential intensity is then given by

$$v' = \{(q'_{+45})^2 + (q'_{-45})^2 - (u')^2\}^{\frac{1}{2}}, \tag{3}$$

where q'_α is the turbulence intensity in the direction α (deg) to the axial direction.

Three experiments for checking system operation and data accuracy were performed. The first provided data for comparison with the classical single-phase turbulent pipe-flow data of Laufer (1954). As figures 6 and 7 demonstrate, agreement is excellent. The second and third experiments were aimed at assuring that light scattered from bubble interfaces was discriminated against and thus not interpreted as a valid liquid-velocity measurement.

When a bubble passes through the laser beams, large amounts of light are scattered, reflected and refracted. Although a high degree of spatial filtering is used, some of this light reaches the photodetector. It is therefore necessary to set up the LDV processor so that the light scattered by bubbles is not interpreted as liquid phase velocity. The LDV signal from the photomultiplier tube is amplified, and if the signal is above a set amplitude limit the signal is rejected. Signals of acceptable amplitude are band-pass filtered to remove both high- and low-frequency noise. The filtered signal then passes to a multi-level Schmidt trigger for future discrimination of unacceptable signals. (For details of the Schmidt trigger see Durst, Melling & Whitelaw (1976) and the TSI MODEL 1990 Instruction Manual.) Both four and eight cycles of the Schmidt trigger signal are timed and compared. The time for eight cycles must be within 1 % of twice the time for four cycles or the signal is rejected. When a signal passes the various checks, a data-ready pulse is output and the analog output corresponding to velocity is updated. The data-ready pulse is used to control the A/D sampling of the computer. That is, the computer samples the analog output of the LDV processor *only on the occurrence of a data-ready pulse*. In between data-ready pulses the analog output stays constant. To check the various settings of the LDV processor, a bubble was introduced into a tube containing downward-flowing water. By adjusting the water flow rate, a balance between the upward buoyancy force and downward drag on the bubble could be achieved and the bubble would remain stationary in the tube. In this manner the bubble could be made to pass through the LDV probe volume extremely slowly and the LDV signal-time segments corresponding to the bubble and a small volume of liquid around it affected by its presence could be greatly expanded for careful examination. The results of such tests are shown in the pictures of figure 2. Note that, in the oscilloscope pictures of the analog signal, velocity data is taken on data-ready pulses. Since the analog output is held constant between data-ready pulses, straight-line segments on the oscilloscope pictures *represent regions where no data is taken*. The pictures of velocity data versus time show the pipe flow ahead of the bubble decreasing as the stagnation point of the bubble approaches the LDV probe volume and then a region of no signal (indicated by no change in velocity) when the bubble intersects the beams. *After the bubble passes, large fluctuations in the wake of the bubble are observed.* While the bubble is in the probe volume the large amount of scattered light causes an occasional datum point to be accepted. However, as can be seen in figure 2, this occurrence is insignificant compared to the data rate when the bubble is not present.

An estimate of the bubble-induced velocity fluctuations was found by examining the effect of a small number of bubbles on the velocity at the centre of a pipe flow.

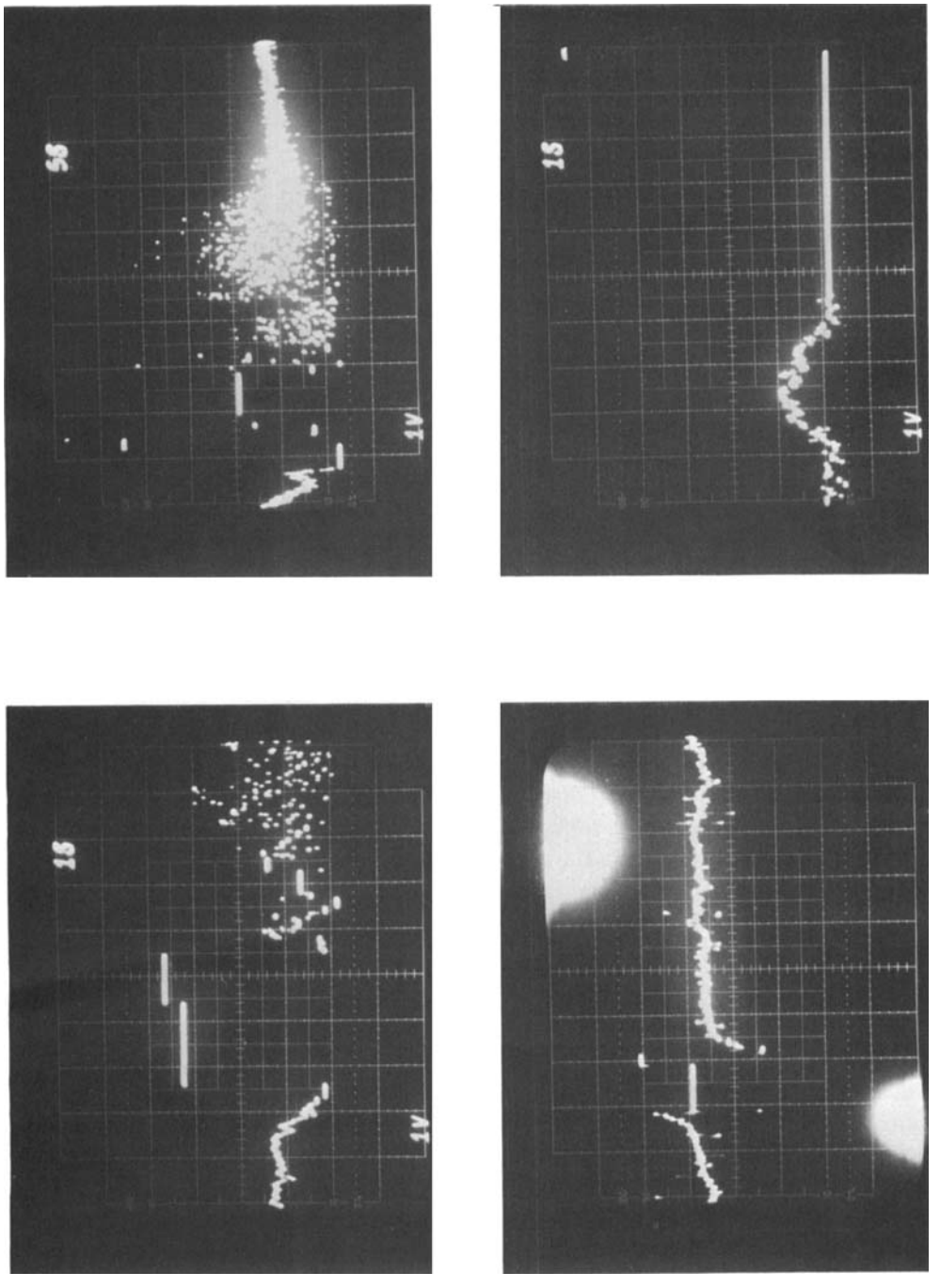

FIGURE 2. Velocity data signal (see text for interpretation) for a gas bubble moving slowly through the LDV probe volume. Scale divisions are 7 cm/s (velocity), 1 s (time).

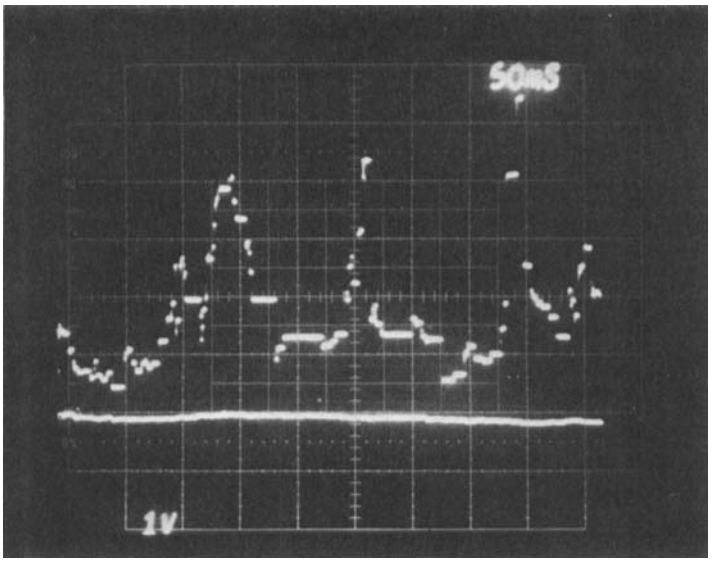

FIGURE 3. Comparison of velocity data signals (see text for interpretation) for laminar flow without (solid line) and with gas bubbles ($\alpha < 0{\cdot}005$). Scale divisions are 7 cm/s (velocity), 50 ms (time).

Figure 3 shows the velocity signal for this case. The solid curve represents the velocity signal prior to the introduction of any bubbles, where the flow is essentially laminar. The introduction of a few bubbles (void fraction less than 0·005) leads to large fluctuations of the velocity as shown in the figure. Individual bubble events are evident as well as events due to groups of bubbles. The bubble rise velocity is estimated as (Wallis 1969) $U_r = 30$ cm/s. Since the liquid velocity at the forward stagnation point of the bubble is equal to $U_r + U$, the maximum measured velocity should be approximately $U_r + U$, and the LDV measurements indicate that this is indeed the case. That is, for the conditions corresponding to figure 3, the maximum velocity is estimated to be 36 cm/s, which is close to the maximum velocity measured. The time for a bubble (of diameter D_B) to pass the measuring point is

$$t_B = \frac{D_B}{U_r + U} \simeq 10 \text{ ms}. \tag{4}$$

Thus the large events at the centre and at the right of figure 3 correspond to single bubbles passing very close to the laser measuring point. Both the sharp rise in velocity in front of the bubble and the fall behind the bubble are evident. The event at the left of figure 3 is most probably caused by several bubbles in the vicinity of the sample volume at the same time. This is evident from the double peak.

Examples of the data for bubbly flow in the pipe are shown in figure 4. Figure 4 (*a*) shows the turbulent pipe flow and figure 4 (*b*) the flow after bubbles are added. Again the effects of bubbles are evident.

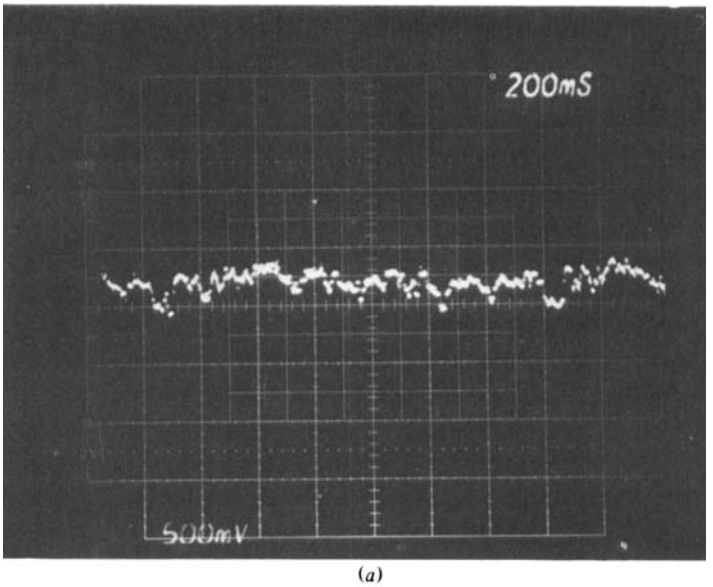

(*a*)

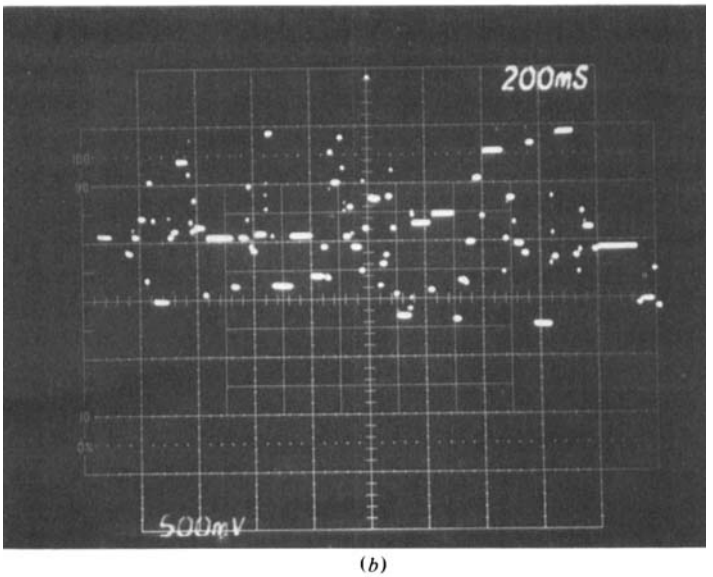

(*b*)

FIGURE 4. Velocity data signals (see text for interpretation): (*a*) at the centre of turbulent pipe flow with $U_m = 46$ cm/s, $u'/U_m = 0{\cdot}057$; (*b*) at the centre of turbulent two-phase bubbly flow with $U_m = 55$ cm/s, $u'/U_m = 0{\cdot}212$, $\chi = 9{\cdot}3 \times 10^{-5}$. Scale divisions are 14 cm/s (velocity), 200 ms (time).

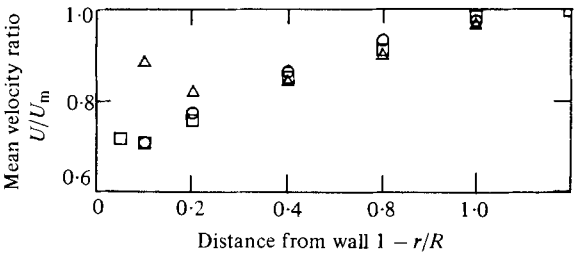

FIGURE 5. Mean axial velocity distribution: ○, single-phase with $U_m = 27$ cm/s; △, two-phase with $U_m = 25$ cm/s and $\chi = 3{\cdot}69 \times 10^{-5}$; □, two-phase with $U_m = 56$ cm/s and $\chi = 9{\cdot}3 \times 10^{-5}$.

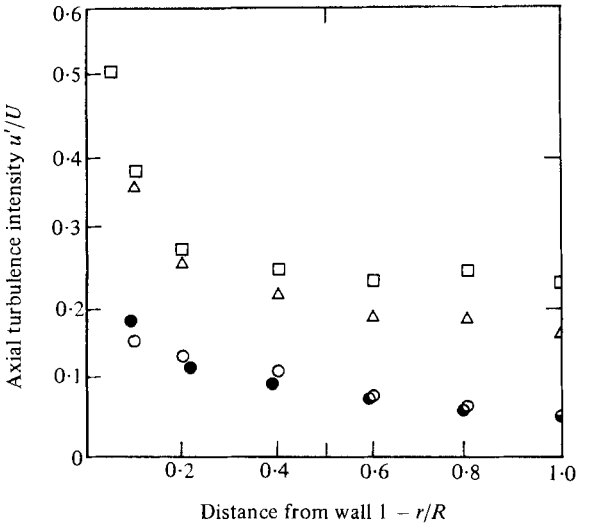

FIGURE 6. Axial-relative-intensity distribution. ●, Laufer's (1954) data.

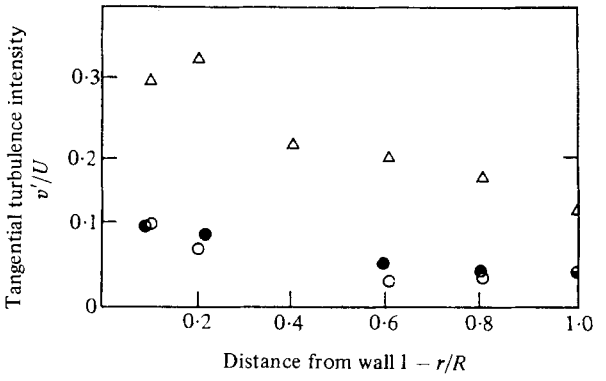

FIGURE 7. Tangential-relative-intensity distribution. ●, Laufer's (1954) data.

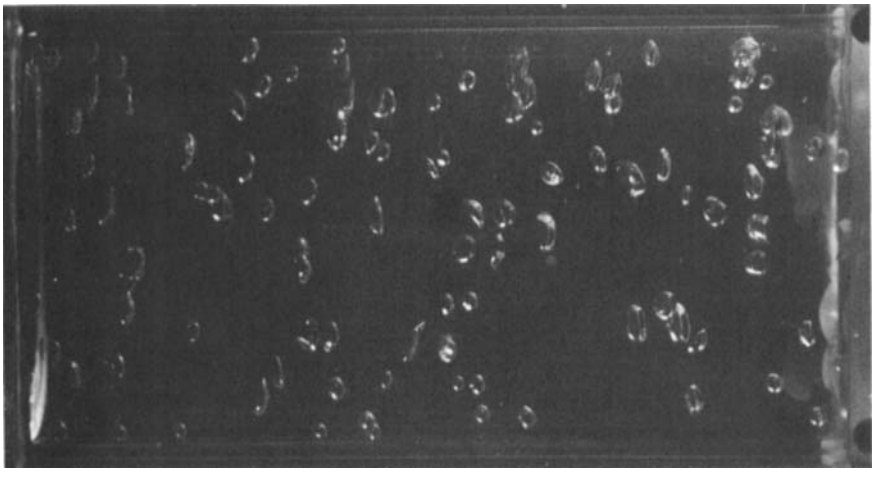

FIGURE 8. Strobe photograph of bubbly pipe flow at $\chi = 2{\cdot}33 \times 10^{-5}$.

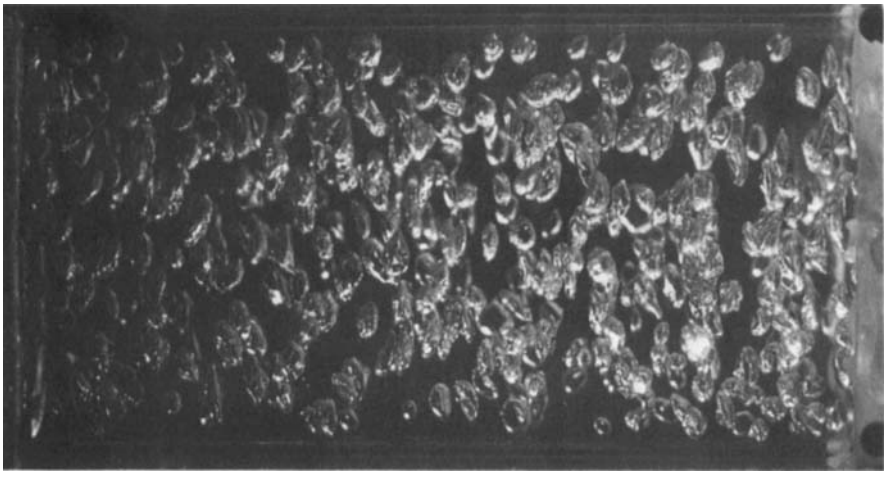

FIGURE 9. Strobe photograph of bubbly pipe flow at $\chi = 9{\cdot}3 \times 10^{-5}$.

4. Experimental results

Mean-velocity profiles for the two-phase conditions are compared to the single-phase velocity profile in figure 5. The profiles are similar in the central portion of the flow (approx. 70% radius). However, significant departures are observed near the wall. These departures may be attributed to the radial phase separation well known for low-quality vertical bubbly flows. Presumably the higher void fraction observed near the wall 'drives' the liquid in a chimney-like effect. This effect appears to diminish at high void fractions where this tendency for preferential wall-void-fraction peaking also diminishes. Serizawa *et al.* (1975*a*, *b*, *c*) did not observe this phenomenon and disputed Malnes' (1966) measurements, attributing the observation to wall and void-fraction interference with the Pitot tube utilized in these later experiments. In view of the completely unobstructive laser technique utilized in our experiments, the

Run no.	Quality $\chi \times 10^4$	Centre-line mean axial velocity U_m (cm/sec)	u'/U_m (%)
1	0·000	45·84	5·74
2	0·465	47·28	17·88
3	0·887	51·30	23·16
4	0·930	54·78	23·45
5	1·770	59·73	24·39
6	2·210	61·95	24·69
7	0·369	23·67	26·61
8	0·738	26·16	34·40
9	1·110	27·00	38·88
10	1·470	27·30	46·05

TABLE 1. LDV data (at the centre-line) in turbulent bubbly flow

reservations of Serizawa *et al.* would appear unfounded. On the other hand Serizawa *et al.* only approached the wall to within 20 % of the radius, thus leaving the major portion of the region of interest, with regard to this phenomenon, unexplored.

The radial variation of the axial intensity u' is shown for two quality conditions in figure 6. As expected, the relative intensity increases near the wall, and the effect of bubbles is seen to be essentially additive to the wall-shear-generated turbulence. The large augmentation of turbulence seen is contrary to the trends observed in Serizawa *et al.* Figure 7 shows the first available data on tangential (θ-direction) intensity. These data follow the general characteristics of the axial intensity and indicate a substantially isotropic behaviour in agreement with the behaviour postulated by Drew & Lahey (1978) to explain radial phase distributions.

Centre-line axial turbulence intensities were obtained for two series of runs at a number of different qualities. Representative two-phase flow structures for the two extrema of low and high qualities investigated are presented in figures 8 and 9. These data are summarized in table 1.

5. Analysis

It is interesting now to examine whether such large bubble contributions to the liquid intensity as we measured may be expected on theoretical grounds. As we have already discussed in §3, such behaviour is caused by the relative velocity (slip) and associated shear. The resulting agitation (turbulence) may therefore be thought of as 'buoyancy-driven' turbulence (or 'gravity-driven' for particulate flow with solids heavier than the fluid). On the other hand, for pipe flow we also have to consider the turbulence due to the wall shear. We will refer to this as 'wall-generated' turbulence. The net result of the interaction between these two modes of turbulence-energy production will depend on their relative magnitude (intensities), their scales, and the extent of any additional dissipative mechanisms due to the presence of a second dispersed phase.

On intuitive grounds we expect an additive behaviour if the two integral length scales are of the same order. The length scale l_w for the major central portion of turbulent pipe flow is 8 % of the diameter, while the particles (bubbles) would create

turbulence of their own size. This would appear to be the case for ours as well as the data of Serizawa *et al.* with $l_w \simeq 0{\cdot}4$ cm and $l_B \simeq 0{\cdot}3$–$0{\cdot}4$ cm. On the other hand, should the particles be too small compared to l_w their contribution might even be dissipative, since a higher effective viscosity and/or a mechanism for break-up of the large eddies is implied. The turbulence intensity for the central major portion of single-phase pipe remains at about 5% of the flow velocity, while the intensity due to suspended particles should increase with their slip velocity and their volume fraction. Other dissipative mechanisms such as those due to surface and/or volume deformations (i.e. surface-tension and compressibility effects) may be envisioned; however, for normal highly turbulent flow their effect will be judged to be of secondary importance. Our concern, therefore, is to formulate an expression for 'buoyancy-driven' turbulence augmentation as described above.

Derivations

In a two-fluid one-dimensional approach, the balance of forces for each phase, per unit volume, yields

$$-\tilde{\boldsymbol{\tau}}_i - \alpha\nabla p + \alpha\rho_d \mathbf{g} = 0, \tag{5}$$

$$\tilde{\boldsymbol{\tau}}_i - (1-\alpha)\nabla p + (1-\alpha)\rho_c \mathbf{g} - \boldsymbol{\tau}_w = 0, \tag{6}$$

where

$$\tilde{\boldsymbol{\tau}}_i \equiv \frac{2c_d \alpha\rho_c}{D_d} |\mathbf{U}_r| \mathbf{U}_r, \tag{7}$$

$$\tilde{\boldsymbol{\tau}}_w \equiv \frac{2c_f(1-\alpha)\rho_c}{D} |\mathbf{U}_c| \mathbf{U}_c \tag{8}$$

are the interfacial and wall shear stresses, respectively. Here, α is the dispersed-phase volume fraction, p the pressure, ρ the density, $\mathbf{g}$ the gravitational acceleration, c_d, c_f the fanning-friction factors, D the pipe diameter and $\mathbf{U}_r = \mathbf{U}_d + \mathbf{U}_c$ is the relative (slip) velocity of the dispersed phase (the subscripts c, d stand for continuous and dispersed phase).

We can eliminate the pressure gradient to obtain

$$\tilde{\boldsymbol{\tau}}_i = \alpha\tilde{\boldsymbol{\tau}}_w - \alpha(1-\alpha)(\rho_c - \rho_d)\mathbf{g}. \tag{9}$$

Hence the total shear force on the liquid (per unit volume of the two-phase field) can be written as:

$$\tilde{\boldsymbol{\tau}}_T = \tilde{\boldsymbol{\tau}}_i + \tilde{\boldsymbol{\tau}}_w = (1+\alpha)\tilde{\boldsymbol{\tau}}_w - \alpha(1-\alpha)(\rho_c - \rho_d)\mathbf{g}. \tag{10}$$

We express this equation *per unit area of tube wall*, by multiplying through by $\frac{1}{4}D$, so that we can use the familiar definition of the shear velocity,

$$u_w^* = \left(\frac{\tau_w}{\rho_c}\right)^{\frac{1}{2}} = [\tfrac{1}{2}c_f(1-\alpha)]^{\frac{1}{2}} U_c, \tag{11}$$

in the result

$$\boldsymbol{\tau}_T = \boldsymbol{\tau}_i + \boldsymbol{\tau}_w = (1+\alpha)\boldsymbol{\tau}_w - \tfrac{1}{2}\alpha(1-\alpha)(\rho_c - \rho_d)R\mathbf{g}, \tag{12}$$

where R is the pipe radius. Thus for bubbly upflow and downflow we have respectively

$$u_T^{*2} = (1+\alpha)u_w^{*2} + \tfrac{1}{2}\alpha(1-\alpha)\left\{1 - \frac{\rho_g}{\rho_l}\right\} Rg, \tag{13}$$

$$u_T^{*2} = (1-\alpha)u_w^{*2} + \tfrac{1}{2}\alpha(1-\alpha)\left\{1 - \frac{\rho_g}{\rho_l}\right\} Rg, \tag{14}$$

where ρ_g, ρ_l are the gas and liquid densities. When the dispersed phase is heavier, such as in the case of solid (or liquid) particles in a gas flow, the corresponding equations are

$$u_T^{*2} = (1-\alpha)\, u_w^{*2} + \tfrac{1}{2}\alpha(1-\alpha)\left\{\frac{\rho_p}{\rho_g} - 1\right\} Rg, \tag{15}$$

$$u_T^{*2} = (1+\alpha)\, u_w^{*2} + \tfrac{1}{2}\alpha(1-\alpha)\left\{\frac{\rho_p}{\rho_g} - 1\right\} Rg, \tag{16}$$

where ρ_p is the density of the particles. Now we see that in the limit $\alpha \to 0$ the total shear velocities approach the wall shear velocity, which in turn, as is well known, will approach the turbulence intensity, i.e.

$$u_T^* \to u_w^* \to u'. \tag{17}$$

This latter limit is a well-known empirical fact which motivates us *to set*

$$u' = u_T^*, \tag{18}$$

even outside the limit $\alpha \to 0$. In doing so, however, we should introduce a parameter to take into account the change in the radial distribution of the turbulence energy. Such change of the distribution, in the direction of increased uniformity, is observed in the experimental data and is consistent with both increased radial diffusion as well as with the additional, volume-distributed, sources of turbulence energy. The simplest choice, then, is to multiply the buoyancy term in (13)–(16) by a constant factor δ, a value to be determined experimentally. We expect this distribution parameter to be of order unity and universal. It is also evident that in a more elaborate effort, taking into account the radially distributed production as well as dissipation and transport, this distribution parameter could be predicted.

The final result may be summarized as

$$\left(\frac{u'}{U_c}\right)^2 = \tfrac{1}{2}c_f(1 \pm \alpha)(1-\alpha) + \delta\alpha(1-\alpha)\left|1 - \frac{\rho_d}{\rho_c}\right| \frac{Rg}{2U_c^2}, \tag{19}$$

with the choice of signs to be made for each particular case from (13)–(16). Since for many flows the quality rather than the void fractions are measured, (19) must be utilized in conjunction with

$$\alpha = \frac{\chi\rho^*}{\chi\rho^* + (1-\chi)\, k}, \tag{20}$$

where

$$\rho^* = \frac{\rho_c}{\rho_d} \quad \text{and} \quad k = \frac{U_d}{U_c} = 1 \pm \frac{U_r}{U_c}, \tag{21}$$

where the signs must be deduced from (7), depending upon the components and flow direction.

In a slightly different interpretation we may proceed by re-expressing (10) per unit area of all shear surfaces (i.e. including that of the dispersed phase). That is, we need to multiply by

$$\tfrac{1}{4}D\left\{1 + 1{\cdot}5\alpha\frac{R}{R_d}\right\}^{-1}, \tag{22}$$

where R_d is the radius of the dispersed phase. The derivation carries through in an exactly parallel fashion and the final result corresponding to (19) is

$$\left(\frac{u'}{U_c}\right)^2 = \left\{\tfrac{1}{2}c_f(1\pm\alpha)(1-\alpha)+\delta\alpha(1-\alpha)\left|1-\frac{\rho_d}{\rho_c}\right|\frac{Rg}{2U_c^2}\right\}\left(1+1{\cdot}5\alpha\frac{R}{R_d}\right)^{-1}. \tag{23}$$

Alternative approaches based on the rate of energy dissipation are also possible. One of the referees noted the similarity of (19) to the expression for the dissipation rate of Kada & Hanratty (1960), and suggested that a dissipation-centred argument would imply weighing our buoyancy term by the relative- to the continuous-velocity ratio. In another, more straightforward way, the well-known relation $\epsilon \sim u'^3/l$ (Batchelor 1953) could be utilized to obtain u'. A detailed discussion of these alternatives, their relation to the available experimental data, and the possible means to experimentally distinguish between them is presented in the appendix.

Asymptotic limits

In evaluating the relative merits of (19) and (23) it is instructive to examine certain asymptotic limits.

(*a*) For $\alpha \to 0$ both equations yield the required result that $u'/U_c \to 0{\cdot}05$ (the value $c_f \simeq 5\times10^{-3}$ is used).

(*b*) For dispersed flows, α is still well below unity (i.e. $\alpha < 0{\cdot}3$), since higher values of α would yield flow-regime transitions to spatially non-homogeneous patterns due to local phase segregation. The region of dominance of channel-wall-generated turbulence may be expressed for both equations as

$$\frac{U_c}{(R_d g)^{\frac{1}{2}}} \gg \left\{\frac{\delta}{c_f}\alpha\left|1-\frac{\rho_d}{\rho_c}\right|\right\}^{\frac{1}{2}}. \tag{24}$$

For typical values of both gas/liquid and solid/gas flows and, say, $\alpha \simeq 0{\cdot}3$, this amounts to

$$U_c \gg O(10(R_d g)^{\frac{1}{2}}). \tag{25}$$

(*c*) In the region of parameters where buoyancy-driven turbulence dominates, however, an essentially different behaviour between the two predictions emerges. From (19) we see that the characteristic velocity is related to the channel dimension (i.e. $(Rg)^{\frac{1}{2}}$), while according to (23) it is related to the dispersed-phase dimension (i.e. $(R_d g)^{\frac{1}{2}}$). Intuitively the latter is a more appealing result. Specifically, in this limit we have (with the values $\delta \simeq 2$ and $4{\cdot}5$ as deduced in the following) from (19) and (23) respectively

$$\frac{u'}{(R_d g)^{\frac{1}{2}}} = \left\{\alpha(1-\alpha)\left|1-\frac{\rho_d}{\rho_c}\right|\right\}^{\frac{1}{2}}, \tag{26}$$

$$\frac{u'}{(R_d g)^{\frac{1}{2}}} = 2{\cdot}25\left\{\alpha(1-\alpha)\left|1-\frac{\rho_d}{\rho_c}\right|\right\}^{\frac{1}{2}}\left\{1{\cdot}5\alpha+\frac{R_d}{R}\right\}^{-\frac{1}{2}}. \tag{27}$$

As the channel radius increases, (26) shows a continuous increase in u' while (27) yields a definite bound, i.e. for $R_d/R \ll \alpha$ we have

$$\frac{u'}{(R_d g)^{\frac{1}{2}}} = 0{\cdot}82\left\{(1-\alpha)\left|1-\frac{\rho_d}{\rho_c}\right|\right\}^{\frac{1}{2}}. \tag{28}$$

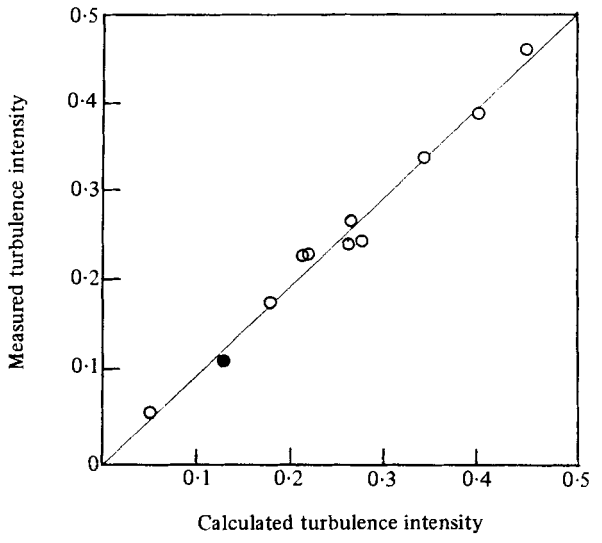

FIGURE 10. Comparison between theoretical predictions (19), with $\delta = 2$, and experimental results from gas/liquid and solid/gas systems: ○, present bubbly flow data; ●, Lee & Durst (1980) solid/gas flow data.

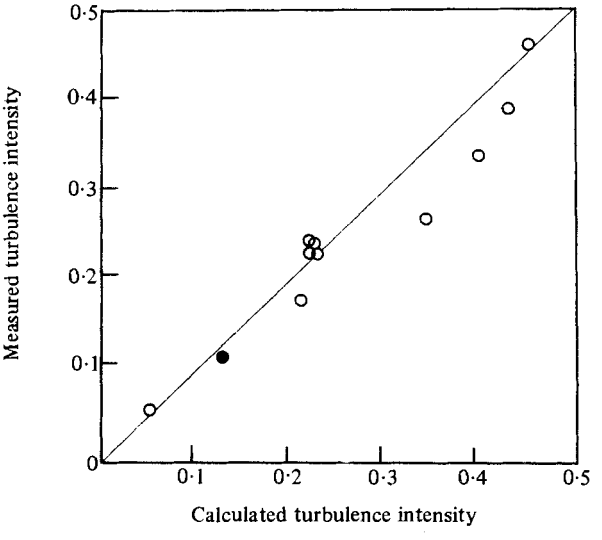

FIGURE 11. Comparison between theoretical predictions (23), with $\delta = 4{\cdot}5$, and experimental results from gas/liquid and solid/gas systems.

For example, for free bubbling with $\rho_d \ll \rho_c$ the intensity is $O(R_d g)^{\frac{1}{2}}$. This conclusion appears reasonable and in agreement with intuition. A little more difficult to visualize is the predicted independence of u' on the void fraction α. This is contrary to the behaviour predicted by (26) and it might eventually provide the means to determine the more sound approach. As we will see in the next section, the presently available data favour (slightly) the former approach (equation (19)).

Application to experimental data

Interpretation of our experimental data in terms of (19) and (23) indicate a value of the distribution parameter of 2 and 4·5, respectively. The value of $R_d \simeq 0{\cdot}2$ cm as determined from photographic records (i.e. figures 8 and 9) was utilized in (23). A bubble-rise velocity of approx. 30 cm/s is estimated (Wallis 1969) and utilized in (20) for relating the void fraction α to the experimentally measured quality χ. For our experimental conditions we have also used $\rho^* = 833$ and $c_f = 0{\cdot}005$. The predictions are compared with the experimental results in figures 10 and 11 for each of the two formulations.

Lee & Durst (1980) report relative intensities for one experimental run in glass-particle/air flow. Their experimental conditions in our nomenclature are: $R = 2{\cdot}09$ cm, $R_d = 0{\cdot}08$ cm, $U_m = 566$ cm/s, $\alpha = 1{\cdot}21 \times 10^{-3}$, and $\rho^* = 5{\cdot}5 \times 10^{-4}$. Just as in our measurement, the radial distribution of the turbulence intensity was found to be substantially flat, in comparison to the single-phase result. A relative intensity value of 11·5 % was determined for this flat portion. Our predictions with (19) and (23), and the same value of the distribution parameter established before, are shown in figures 10 and 11, respectively.

It should be noted that the above experimental situations are not truly one-dimensional. In applying our one-dimensional approximation we have taken into account the difference between the centre-line, U_m, and radial-average, U_c, velocities, by appropriately renormalizing (19) and (23) (by the centre-line velocity U_m).

6. Discussion

Considering the rather extreme range of conditions spanned by these two experiments, the unifying power of the theory and the universality of the value assigned to the distribution parameter δ are evident. It is also worth noting that for our experiments

$$U_c \ll 10(Rg)^{\frac{1}{2}}, \tag{29}$$

and the data provide a test of the theory in the domain dominated by buoyancy-driven turbulence, i.e. (26) or (27) apply. On the other hand, for the experiment of Lee & Durst

$$U_c \sim O(10(Rg)^{\frac{1}{2}}), \tag{30}$$

and their data provide a test of the theory in the intermediate range where the wall-generated turbulence begins to become important.

For low-pressure air/water bubbly flows, $\rho_d \ll \rho_c$, $U_r \simeq 30$ cm/s, $\alpha \ll 1$, and $\chi\rho^* < 1$, and (19)–(21) yields

$$\frac{u'}{U_c} \simeq \left\{\tfrac{1}{2}c_f + \chi\rho^*\left(1+\frac{U_r}{U_c}\right)^{-1}\frac{Rg}{U_r^2}\left(\frac{U_r}{U_c}\right)^2\right\}^{\frac{1}{2}}; \tag{31}$$

that is, for a given geometry and pressure level the relative intensity is only a function of the quality χ and the velocity ratio U_r/U_c. The rather strong dependence on both of these parameters is illustrated graphically in figure 12. The exact solution, (19)–(21), rather than the simplified equation (31), is presented. In terms of the velocity ratio, our data are characterized by $0{\cdot}6 < U_r/U_c < 1{\cdot}5$ and the data of Serizawa *et al.*

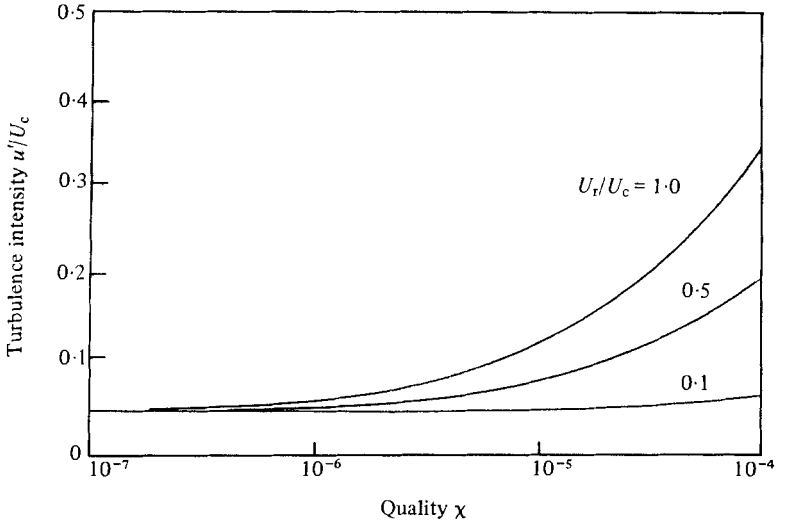

FIGURE 12. Illustration of the variation of relative intensity with quality and velocity ratio U_r/U_c, for low-pressure, gas/liquid, bubbly upflow. Equation (19) with $\delta = 2$.

(1975*a*, *b*, *c*), with the exception of two points, by $0{\cdot}22 < U_r/U_c < 0{\cdot}40$. With reference to figure 12, we expect significantly different relative intensities for the two essentially disjoint U_r/U_c regions characteristic of these two data sets. Indeed the intensities of Serizawa *et al.* are significantly lower than ours. However, the actual measurements are also significantly lower than the predicted values (typically by factors of 2 to 3). Furthermore, again contrary to the predictions (and our data), no significant sensitivity to the quality was observed. The reason for these discrepancies is not clear at this time. The rather limited extent in the range of low qualities, i.e. $\chi < 10^{-4}$, investigated by Serizawa *et al.* imposes some difficulties in evaluating the experimental trends. On the other hand they reported data indicating 'a systematic increase of diffusivity of heat E_H with quality and water velocity', a trend that is more consistent with our turbulence-intensity results than with their own. On the other hand our centre-line velocities increase with quality (table 1) precisely as those measured by Serizawa *et al.* and provide further evidence of the reliability of our laser data in a bubbly flow.

7. Conclusions

A theoretical basis for the prediction of turbulence levels in two-phase flows has been proposed and shown to be useful in providing a unified interpretation of experimental data in the extremely diverse systems of bubbly gas/liquid, and particulate-solids/gas two-phase flows. The asymptotic limits discussed, together with the theoretically predicted parametric trends, do point to the need for, as well as the direction of, future experimental work for evaluating the theory in the ranges not covered by the presently available experimental data.

This work was supported in part by NSF Grant no. 7521700A1. We would like to thank Mr J. Beecher for helping with the experiments.

Appendix

The expression for the dissipation rate as given by Kada & Hanratty (1960) for turbulent, slurry pipe flow is, in our nomenclature,

$$\epsilon = \left\{1+\alpha\frac{U_r}{U_c}\right\}\frac{2\tau_w U_c}{(1-\alpha)\rho_c R} - \alpha\frac{\rho_d-\rho_c}{\rho_c}gU_r. \tag{A 1}$$

We rearrange and generalize this into the form suggested by (13)–(16) and (19) to obtain

$$\tfrac{1}{2}(1-\alpha)R\frac{\epsilon}{U_c} = \left(1\pm\alpha\left|\frac{U_r}{U_c}\right|\right)\frac{\tau_w}{\rho_c} + \alpha(1-\alpha)\left|1-\frac{\rho_d}{\rho_c}\right|\frac{Rg}{2U_c^2}\left|\frac{U_r}{U_c}\right|. \tag{A 2}$$

In the limit $\alpha\to 0$, $\tau_w/\rho_c \to u'^2$, and the left-hand side of (A 2) may be interpreted in general as u_T^{*2} in the sense of (17) and (18). That is

$$\left(\frac{u'}{U_c}\right)^2 = \tfrac{1}{2}c_f\left(1\pm\alpha\left|\frac{U_r}{U_c}\right|\right)(1-\alpha)+\alpha(1-\alpha)\left|1-\frac{\rho_d}{\rho_c}\right|\frac{R_g}{2U_c^2}\left|\frac{U_r}{U_c}\right|, \tag{A 3}$$

which is just like (19) except for the U_r/U_c weighting, as indicated. From (A 2) and (A 3) we also have

$$\frac{u'}{U_c} = \left\{\tfrac{1}{2}(1-\alpha)R\frac{\epsilon}{U_c^3}\right\}^{\frac{1}{2}}. \tag{A 4}$$

The dissipation rate (A 1) may also be utilized in conjunction with $\epsilon \simeq u'^3/l$ to estimate the intensity. As discussed in §5, at least for the conditions for which experimental data exist, we may take $l \sim l_B \sim 2R_d$ to obtain

$$\frac{u'}{U_c} = \left\{\frac{2R_d\epsilon}{U_c^3}\right\}^{\frac{1}{3}}. \tag{A 5}$$

This equation may be utilized with (A 1) to estimate the intensity. It is more instructive, however, to obtain the relation between the two estimates provided by the two dissipation-based approaches, i.e. (A 3) and (A 5). Elimination of ϵ/U_c^3 between (A 4) and (A 5) yields

$$\left(\frac{u'}{U_c}\right)_{A5} = \left(\frac{u'}{U_c}\right)_{A3}^{\frac{2}{3}}\left\{\frac{4R_d}{(1-\alpha)R}\right\}^{\frac{1}{3}}. \tag{A 6}$$

This relation is shown graphically in figure 13 for the experimental conditions of Lee & Durst (1980) and of our data. In the small void-fraction range of interest the liquid-fraction dependence was neglected in this particular graphical presentation.

It is interesting to note that Lee & Durst's point happens to fall, owing to the particular choice of R_d/R in this experiment, very close to the intersection with the 45° line; i.e. these two approaches would predict essentially the same results. A modest discrimination capability is indicated for u'/U_c up to 0·20. That is, much stronger buoyancy-driven turbulence conditions must be utilized before the high-discrimination region of $u'/U_c > 0{\cdot}2$ may be achieved. For the experimentalist another possibility would be to choose the R_d/R ratio such that the whole curve in figure 13 shifts as much as possible. Owing to the cube-root dependence of this factor in (A 6), however, this approach has its own limitations. In particular, caution must be exercised as $R_d/R \to 0$, since at some point the separation of length scales between

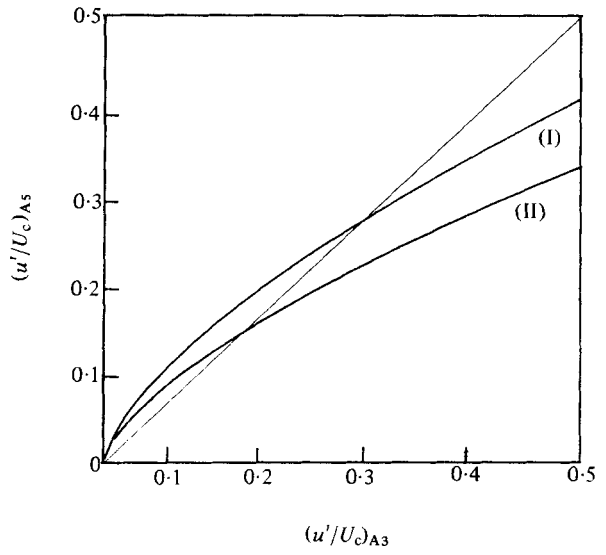

FIGURE 13. Comparison between the intensity predictions of the two dissipation-based approaches: (I) behaviour typical of our bubbly-flow data, with $R_d = 0{\cdot}2$ cm and $R = 2{\cdot}85$ cm; (II), behaviour typical of the Lee & Durst (1980) particulate-flow data, with $R_d = 0{\cdot}08$ cm and $R = 2{\cdot}09$ cm.

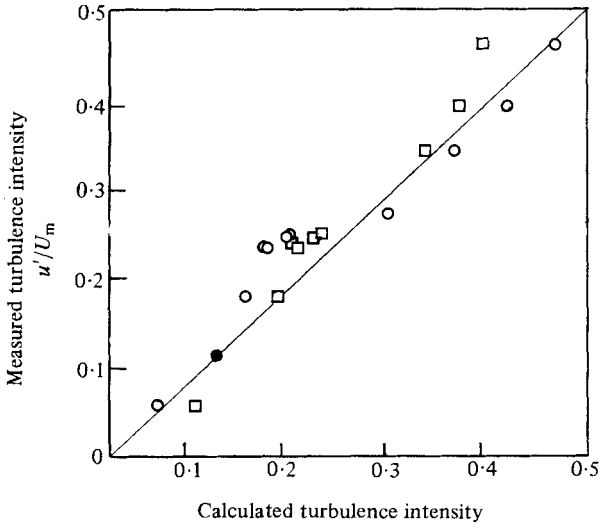

FIGURE 14. Comparison between the experimental data and theoretical predictions of dissipation-based models: ○, present bubbly-flow data and equation (A 3); □, present bubbly-flow data and equations (A 1) and (A 5); ●, the Lee & Durst (1980) data point (both predictions essentially the same).

wall- and buoyancy-generated turbulence may be significant, making the choice of l problematical. One way out of this dilemma would be to choose the flow conditions such that the buoyancy term in (A 1) clearly dominates, and then use $l \sim l_B = 2R_d$.

As seen in figure 13, for bubbly flows the discriminating power of (A 6) is good, except in the narrow range around $u'/U_c \simeq 0{\cdot}29$, and it could be clearly improved by appropriate choices for R_d and R. A more direct illustration of the trends shown in

figure 13, together with a demonstration of the effect of the U_r/U_c weighing in (A 3) (relative to (19)) is provided in figure 14. First we note that the predictions of (A 3) are very good in the range $0{\cdot}29 < u'/U_c < 0{\cdot}50$, but a systematic underprediction is observed, for the bubbly-flow data, in the range $0{\cdot}1 < u'/U_c < 0{\cdot}29$. The use of (A 5), on the other hand, improves the prediction in the lower range but worsens it in the higher one. Notwithstanding these apparently systematic trends, the quality of comparisons in figure 14 is not bad and it should not lead to the conclusion that the U_r/U_c weighing is without merit. Considering the ranges of U_r/U_c values for which the data in figure 14 were obtained, i.e.

$$0{\cdot}6 < \frac{U_r}{U_c} < 1{\cdot}5 \quad \text{for the bubbly flow,}$$

$$\frac{U_r}{U_c} = 0{\cdot}75 \quad \text{for the particulate flow,}$$

we identify the need for data with U_r/U_c more decisively different from unity. We are currently pursuing this goal.

Finally, it is worth noting that (A 5) does not reduce in the limit $\alpha \to 0$ to the single-phase result. Instead, using $l \simeq 0{\cdot}08D$ for single-phase flow as discussed earlier, we have

$$\frac{u'}{U_c} = \left\{c_f \frac{l}{R}\right\}^{\frac{1}{3}} \simeq 0{\cdot}093.$$

REFERENCES

AKAI, M., INOUE, A. & AOKI, S. 1975 Structure of co-current stratified two-phase flow with wavy interface. *Theor. Appl. Mech.* **25**, 445–456.

AKAI, M., INOUE, A., AOKI, S. & ENDO, K. 1980 A co-current stratified air-mercury flow with wavy interface. *Int. J. Multiphase Flow* **6**, 173–190.

BATCHELOR, G. K. 1953 *The Theory of Homogeneous Turbulence*. Cambridge University Press.

COHEN, L. S. & HANRATTY, T. 1968 Effect of waves at a gas–liquid interface on a turbulent air flow. *J. Fluid Mech.* **32**, 467–479.

DREW, D. & LAHEY, R. J. 1978 Radial phase distribution mechanisms in two-phase flow. *Proc. Symp. on Mechanism of Two-Phase Flow* (in press).

DURST, F., MELLING, A. & WHITELAW, T. H. 1976 *Principles and Practice of Laser Doppler Anemometry*. Academic.

HINZE, J. O. 1955 Fundamentals of the hydrodynamic mechanism of splitting in dispersion processes. *A.I.Ch.E. J.* **1**, 289–295.

HOUZE, R. N. & THEOFANOUS, T. G. 1980 Turbulence and mass transfer in multiphase flows. PCHE 81-1, Purdue University.

JEFFRIES, R. B., SCOTT, D. S. & RHODES, E. 1969*a* The structure of turbulence close to the interface in the gas phase of a co-current stratified two-phase flow. In *Proc. Symp. on Mechanics of Two-Phase Flow, A.I.Ch.E. 66th Nat. Meeting, Portland, Oregon.*

JEFFRIES, R. B., SCOTT, D. S. & RHODES, E. 1969*b* Structure of turbulence close to the interface in the liquid phase of the co- current stratified two-phase flow. In *Proc. Symp. Fluid Mech. and Measurements in Two-Phase Flow Systems, Leeds, England.*

KADA, H. & HANRATTY, T. J. 1960 Effects of solids on turbulence in a fluid. *A.I.Ch.E. J.* **6**, 624–630.

LAUFER, J. 1954 The structure of turbulence in fully developed pipe flow. *N.A.C.A. Rep.* 1174.

LEE, S. L. & DURST, F. 1980 On the motions of particles in turbulent flow. *U.S. Nuclear Regulatory Commission Rep.* NUREG/CR-1554.

MALNES, D. 1966 Slip ratios and friction factors in the bubble flow regime in vertical tubes. Institutt for Atomenergi, Kjeller, Norway.

McLaughlin, D. K. & Tiederman, W. G. 1973 Biasing correction for individual realization of laser anemometer measurements in turbulent flows. *Phys. Fluids* **16**, 2082–2088.

Serizawa, A., Katuoka, I. & Michiyoshi, I. 1975*a* Turbulence structure of air-water bubbly flow—I Measuring techniques. *Int. J. Multiphase Flow* **2**, 221–233.

Serizawa, A., Katuoka, I. & Michiyoshi, I. 1975*b* Turbulence structure of air–water bubbly flow—II. Local properties. *Int. J. Multiphase Flow* **2**, 235–246.

Serizawa, A., Katuoka, I. & Michiyoshi, I. 1975*c* Turbulence structure of air–water bubbly flow—III. Transport properties. *Int. J. Multiphase Flow* **2**, 247–259.

Theofanous, T. G. 1975 Horizontal, stratified, gas–liquid flow: The interfacial region. In *Proc. 15th Nat. Heat Transfer Conf., San Francisco, California.*

Theofanous, T. G. 1980 The boiling crisis in nuclear reactor safety and performance. *Int. J. Multiphase Flow* **6**, 60–95.

Theofanous, T. G., Houze, R. N. & Brumfield, L. K. 1976*a* Turbulent mass transfer at free, gas–liquid interfaces, with applications to open-channel, bubble and jet flows. *Int. J. Heat Mass Transfer* **19**, 613–624.

Theofanous, T. G., Houze, R. N., Brumfield, L. K. & Johns, D. M. 1976*b* Structure of free boundary turbulence and interphase mass transport. PCHE 76-1, Purdue University.

Wallis, G. B. 1969 *One-Dimensional Two-Phase Flow.* McGraw-Hill.

Yanta, W. T. & Smith, R. A. 1973 Measurements on turbulence-transport properties with laser–Doppler anemometer. *A.I.A.A. Paper* 73–169.